Pergamon

Computers Math. Applic. Vol. 32, No. 10, pp. 109–124, 1996

0898-1221/96 $15.00 + 0.00

PII: S0898-1221(96)00189-7

Exotic Dynamic Behavior of the Forced FitzHugh-Nagumo Equations

MO-HONG CHOU* AND YU-TUAN LIN
Institute of Mathematics, Academia Sinica
Nankang, Taipei 11529, Taiwan, R.O.C.

(Received November 1995; accepted January 1996)

Abstract—Space-clamped FitzHugh-Nagumo nerve model subjected to a stimulating electrical current of form $I_\circ + I\cos\gamma t$ is investigated via Poincaré map and numerical continuation. If $I = 0$, it is known that Hopf bifurcation occurs when $I_\circ$ is neither too small nor too large. Given such an $I_\circ$. If γ is chosen close to the natural frequency of the Hopf bifurcated oscillation, a series of exotic phenomena varying with I are observed numerically. Let $2\pi\lambda/\gamma$ denote the generic period we watched. Then the scenario consists of two categories of period-adding bifurcation. The first category consists of a sequence of hysteretic, $\lambda \to \lambda + 2$ period-adding starting with $\lambda = 1$ at $I = 0+$, and ending at some finite I, say I_*, as $\lambda \to \infty$. The second category contains multiple levels of period-adding bifurcation. The top level consists of a sequence of $\lambda \to \lambda + 1$, period-adding starting with $\lambda = 2$ at $I = I_*$. From this sequence, a hierarchy of $m \to m + n \to n$, period-adding in between are derived. Such a regular pattern is sometimes interrupted by a series of chaos. This category of bifurcation also terminates at some finite I. Harmonic resonance sets in afterwards. Lyapunov exponents, power spectra, and fractal dimensions are used to assist these observations.

Keywords—FitzHugh-Nagumo equations, Bistability, Period-adding, Chaos.

1. INTRODUCTION

A system formed by the FitzHugh-Nagumo (FHN) equations is known as a simplified model of the Hodgkin-Huxley equations for the nerve membrane [1–5]. When such a system is space-clamped and subjected to a stimulating electrical current shaped by the Heaviside function with a step $I_\circ$, persistent oscillations are observed in certain numerical simulations [4,6] if $I_\circ$ is neither too small nor too large. Given such an $I_\circ$, we are then interested in the consequence of imposing a sinusoidal perturbation of form $I\cos\gamma t$ upon the base current. In the following sections we shall show that, if γ is chosen close to the natural frequency of the unperturbed oscillation, exotic bifurcation phenomena varying with I can take place in a way similar to that in connection with the Van der Pol equation [7,8]. Namely, period-adding is a common route to chaos for these two types of oscillators.

The space-clamped FHN equations with the aforesaid forcing term can be written as

$$u_t = f(u) - v + I_\circ + I\cos\gamma t, \qquad f(u) \equiv -u(u-\alpha)(u-1), \tag{1}$$

$$v_t = \beta(\theta u - v), \qquad t \geq 0 \tag{2}$$

where $0 < \alpha < 1$ and β, γ, and θ are positive parameters. The current parameters $I_\circ, I$ are assumed to be nonnegative.

This work was supported in part by the National Science Council under Grants NSC-84-2121-M-001-023 and NSC-84-2112-M-001-052.
*Author to whom all correspondence should be addressed.

We first recall from our previous work [6] some facts about the case $I = 0$. Let (u^*, v^*) designate a generic steady state of (1) and (2). If

$$\theta \geq \frac{1 - \alpha + \alpha^2}{3} \text{ (single steady state)}, \tag{3}$$

then (u^*, v^*) is unique for any I_o. Otherwise, if

$$\frac{(1-\alpha)^2}{4} < \theta < \frac{1 - \alpha + \alpha^2}{3} \text{ (multiple steady states)}, \tag{4}$$

multiple (u^*, v^*) occur for a certain range of positive I_o. The condition for Hopf bifurcation taking place at (u^*, v^*) is given by

$$f'(u^*) = \beta \quad \text{and} \quad \beta < \theta \text{ (condition for Hopf bifurcation)}, \tag{5}$$

where f is defined in (1). In terms of I_o, the possible bifurcation points are given by

$$I_o^{\pm} = \theta u^{\pm} - f(u^{\pm}), \qquad u^{\pm} = \frac{(1+\alpha) \pm \sqrt{1 - \alpha + \alpha^2 - 3\beta}}{3}. \tag{6}$$

These two points do exist and satisfy $I_o^- < I_o^+$, if β is small enough.

There is a significant difference between the existence of single and multiple steady states. If (3) holds, soft Hopf bifurcation takes place in the sense that stable periodic solutions are found for I_o located in an interval, $\mathcal{H}$, equal to $[I_o^-, I_o^+]$; if (4) holds, this interval $\mathcal{H}$ is somewhat larger. We call the latter case hard Hopf bifurcation in which bistability is present. There is, however, one thing in common that the related periods for either type of bifurcation are in general quite large, if a transition to relaxation oscillation is involved in the course of path-following with varied I_o.

Now, we restore the sinusoidal perturbation $I \cos \gamma t$ to a base current I_o with respect to which the Hopf bifurcated oscillation is known to have period $2\pi T_o$. The perturbation frequency γ is chosen such that $\gamma \cdot T_o = \mathcal{O}(1)$, because subharmonic resonance is expected in this range from the general consideration of nonlinear dynamics. For a more detailed consequence, direct numerical simulation is inevitable.

The numerical methods we used are presented in Section 2. A mixture of global and local analyses is adopted in this work. Section 3 presents several worked examples towards completing a bifurcation diagram which reveals a variety of period-adding phenomena typical to a sinusoidally forced FHN system.

2. DESCRIPTION OF NUMERICAL METHODS

2.1. Poincaré Map and Interpolated Cell Mapping

Over the phase space (i.e., the uv-plane) a uniform grid is constructed to cover a rectangular region containing the possible attractors. Started from each grid point, equations (1) and (2) are integrated numerically for t running from 0 to $2\pi/\gamma$. As noticed above, γ is small in general. Therefore, quality control over such long-term integrations is needed. Numerical solvers of Adams-Gear type such as LSODE [9] and of Runge-Kutta type such as RKF45 [10] are used, and they yield similar accuracy.

To mimic the continuous Poincaré map the grid should be dense enough, and the huge collection of grid points are then traced by repeatedly applying the numerical integration mentioned above. It can be expected that such an integration procedure will become quite expensive eventually.

This burden can be alleviated by the so-called interpolated cell mapping [11]. After constructing the discrete grid map by numerical integration over the first period, we introduce cellwise bilinear interpolation to obtain a continuous version of this map. Denote it by $\mathcal{M}$. A cell, $C_{i,j}$, is a small

rectangular region formed here by four neighboring grid points indexed as (i,j), $(i+1,j)$, $(i,j+1)$, $(i+1,j+1)$. The further evolution of these grid points or any other more suitable set of sample points can be traced hereafter in a way like table look-up, i.e., for any point $\mathbf{x}$ we merely check which (i,j) is such that $\mathbf{x} \in \mathcal{C}_{i,j}$, and then perform the bilinear interpolation $\mathcal{M}(\mathbf{x})$. When a sample point runs out of the domain covered by the grid during the iterated interpolation $\mathcal{M}^n$, it will be discarded simply.

2.2. Periodic Solutions and Simple Cell Mapping

Apply the thus constructed Poincaré map $\wp$ times, where $\wp$ is a big natural number. Certain dynamic patterns may have been revealed by the particular accumulation of the sample phase points. If the system in consideration presents a long transient stage, the desired $\wp$ might be too large to be practical.

An alternative to speed up such a pattern recognition is provided by the so-called simple cell-to-cell mapping [12]. In this regard $\wp$ is restricted to be prime for reason to be clear below, and the sample points, if different from the grid points, are assumed to be located over a rectangular mesh initially.

After $\wp$ times of Poincaré map, the image of each sample point is rounded off to its nearest mesh point. If $\wp = 1$, we return to the original version of simple cell mapping [12]. It is $\wp \gg 1$ that allows us to perform the round-off in a somewhat post-transient stage and to reduce the associated error. By means of this simplification, the $\wp$-stage Poincaré map can be read as $S : \mathcal{Z} \to \mathcal{Z}$ where $\mathcal{Z}$ consists of the first $K+1$ nonnegative integers with K equal to the amount of mesh points. The map S satisfies $S(0) = 0$ and $S^{-1}(0)$ stands for those sample points we have discarded simply because they run outside the grid domain. This setting makes S have at least one periodic solution.

Since it will just involve integer arithmetic, to iterate the map S is quite simple. If S has a periodic solution of period p, the original system may have a correspondent of period p or $p \cdot \wp$ only. This is the reason for $\wp$ being prime. Although some precautions have been taken, it is still possible to obtain spurious results from this speedup process.

2.3. Domains of Attraction and Composite Cell Mapping

When there exist more than one attractors, it is desirable to know their respective domains of attraction. Such a desire is the motif of developing the simple cell mapping method [12], within which an array of indices is generated to point each sample point to the attractor to which it belongs. It sometimes happens that components of different attractors are located closely. To discriminate them, the cell size should be fine enough.

In practice, this is achieved through local refinement by overlaying the critical regions a nest of finer grids. The cellwise interpolation and the round-off procedure as discussed in the preceding sections should be modified accordingly to respect the local cell size. We call this treatment a composite cell mapping.

In conjunction with chaotic dynamics, the high sensitivity to initial conditions may still be overlooked by the careful simplifications introduced thus far. For instance, a chaos is sometimes recognized as several distinct groups of periodic motions with long periods. To improve the capability in this connection, one may employ the so-called generalized cell mapping methods [12,13], at the expense of algorithmic complexity. It, however, seems more straightforward to perform a double check on these well-sorted data by direct numerical integration.

2.4. Path-Following of Periodic Attractors

It is very time-consuming to perform Poincaré map with respect to the continuously varied parameter I, even by means of the simplifications introduced above. Domain decomposition provides an additional means of acceleration in which we partition the (finite) phase plane into

several blocks and then perform the associated maps concurrently, for instance, by a parallel virtual machine (PVM). However, it does not pay to do this tedious work unless for critical I's. By critical we mean a bifurcation is detected, through the local stability analysis, by the path-following process stated below.

To trace periodic attractors with varied I but of fixed period $2\pi T$, $T = \lambda/\gamma$ for some natural number λ, Fourier method is a natural approach. In this connection the FHN equations (1) and (2) can be rewritten as

$$u_t = T\left(f(u) - v + I_o + I\cos\lambda t\right), \tag{7}$$

$$v_t = T\beta(\theta u - v), \qquad 0 \le t \le 2\pi. \tag{8}$$

Now, we seek a solution of (7) and (8) with

$$u(t) = \sum_{k=0}^{K} P_k \cos(kt) + Q_k \sin(kt), \tag{9}$$

where P_k and Q_k are scalar quantities with $Q_0 = 0$ for convenience. By (8), we then have

$$v(t) = \theta \sum_{k=0}^{K} \left[(p_k P_k - q_k Q_k)\cos(kt) + (q_k P_k + p_k Q_k)\sin(kt)\right], \tag{10}$$

where $p_0 \equiv 1$, $q_0 \equiv 0$ and

$$p_k \equiv \frac{(\beta T/k)^2}{1 + (\beta T/k)^2}, \quad q_k \equiv \frac{\beta T/k}{1 + (\beta T/k)^2}, \qquad \text{for } k \ge 1. \tag{11}$$

Substituting (9) and (10) into (7), and then equating like Fourier modes on both sides, a system of nonlinear equations for P_k and Q_k, $0 \le k \le K$, is obtained. Detailed expression can be found in our previous works [6,14]. Such a nonlinear system can be solved by a damped Newton method [15]. Note that the solution will depend on the parameter I, and one can employ the so-called pseudo-arclength continuation techniques [16] to obtain solutions for I over some extension.

When the pursued subharmonic resonance presents a long period, that is $\lambda \gg 1$ in (7), the upper bound, K, for the employed Fourier modes should be increased substantially in order to take account of the periodic forcing term. In these circumstances we suggest using the shooting methods stated below.

For simplicity of discussion, let us put (7),(8) into the following vector form in which all parameters except I are suppressed for the time being.

$$\mathbf{x}_t = \mathcal{F}(\mathbf{x}, t, I), \quad \mathbf{x} = (u, v)^\top, \qquad 0 \le t \le 2\pi. \tag{12}$$

To use a multiple shooting method, the interval $[0, 2\pi]$ is partitioned into M equal subintervals for some prescribed M (far less than the K used by Fourier method). Then, a numerical solver such as LSODE [9] or RKF45 [10] is used to integrate (12) over these M subintervals simultaneously. Their respective initial vectors are denoted by $\mathbf{x}_j$, $0 \le j < M$, and their respective target vectors are denoted by $\mathbf{g}(\mathbf{x}_j, I)$.

The constraints on $\mathbf{x}_j$ for seeking periodic solutions of (12) are

$$\begin{aligned} \mathbf{g}(\mathbf{x}_j, I) &= \mathbf{x}_{j+1}, \qquad \text{for } 0 \le j < M, \\ \mathbf{x}_M &= \mathbf{x}_0. \end{aligned} \tag{13}$$

This system is, again, to be solved by a damped Newton method [15]. Note that numerical integration for the variational equations of (12) now is coupled with, rather than separated from,

the solution process of (13) as compared with Fourier method in which one can compute the related Jacobian analytically.

To be complete, we actually have to integrate, for $0 \leq j < M$, the following augmented system over $j\sigma \leq t \leq (j+1)\sigma$ where $\sigma = 2\pi/M$.

$$\begin{aligned} \mathbf{x}_t &= \mathcal{F}(\mathbf{x}, t, I), & \mathbf{x}(j\sigma) &= \mathbf{x}_j, \\ \mathbf{y}_t &= \mathcal{F}_{\mathbf{x}}(\mathbf{x}, t, I)\mathbf{y}, & \mathbf{y}(j\sigma) &= \begin{pmatrix} 1 & 0 \\ 0 & 1 \end{pmatrix}, \\ \mathbf{e}_t &= \mathcal{F}_{\mathbf{x}}(\mathbf{x}, t, I)\mathbf{e} + \mathcal{F}_I(\mathbf{x}, t, I), & \mathbf{e}(j\sigma) &= \begin{pmatrix} 0 \\ 0 \end{pmatrix}. \end{aligned} \tag{14}$$

The last equation of (14) is relevant to the pseudo-arclength continuation [16]. Let $\mathcal{S}$ denote the product of the variational solutions among different j's. That is

$$\mathcal{S} = \prod_{j=0}^{M-1} \mathbf{y}((j+1)\sigma, I). \tag{15}$$

If $\mathcal{S}$ has an eigenvalue greater than one in modulus, the traced periodic solution is unstable, and we call the corresponding I critical. Poincaré map is called in this case for searching other possible attractors.

2.5. Lyapunov Exponents, Power Spectra, and Fractal Dimensions

According to the above setting, a chaos $\mathcal{A}$ is recognized as one or more periodic attractors with long periods by various cell mapping methods. These attractors, however, fail to be identified by Fourier and shooting methods. To handle this situation certain measures pertinent to chaotic dynamics [17] are needed, along with the direct numerical integration.

To this end, let the FHN equations (1) and (2), together with their first variation, be denoted again as

$$\begin{aligned} \mathbf{x}_t &= \mathcal{F}(\mathbf{x}, t), \\ \mathbf{y}_t &= \mathcal{F}_{\mathbf{x}}(\mathbf{x}, t)\mathbf{y}. \end{aligned} \tag{16}$$

The first measure is the Lyapunov exponents concerning the sensitivity to the initial conditions. For this sake, input $\mathbf{x}(0) = \mathbf{x}_0 \in \mathcal{A}$, $\mathbf{y}(0) = \left(\begin{smallmatrix} 1 & 0 \\ 0 & 1 \end{smallmatrix}\right)$ into (16), and integrate them for sufficiently large time. Let $\mu_1(t), \mu_2(t)$ denote the eigenvalues of $\mathbf{y}(t)$ such that $|\mu_1(t)| \geq |\mu_2(t)|$ for all t. The Lyapunov exponents are defined, in principle, as the limits:

$$\ell_i = \lim_{t \to \infty} \frac{\log |\mu_i(t)|}{t}, \qquad i = 1, 2. \tag{17}$$

However, it is hard to find the existence of these limits in practice. A more feasible approach is to interpret these ℓ_i's in terms of linear correlation. When (17) is extended to cover periodic cases, a useful guess for these ℓ's is given by Floquet multipliers. Namely,

$$\ell_i \approx \frac{\log |\mu_i(T)|}{T}, \qquad i = 1, 2. \quad (T = \text{period}). \tag{18}$$

The second measure consists of power spectra which provide distinct regular patterns for periodic attractors even if their periods are quite large. Aperiodicity can be evidenced by irregular peaks and noise. Let $\{\mathbf{x}_0, \mathbf{x}_1, \ldots, \mathbf{x}_n, \ldots\}$ stand for the intermediate output of integrating (16) at $t = 2\pi n/\gamma$, $n = 0, 1, 2, \ldots$. The power spectrum of this sequence of data is generated by using the signal processing toolbox of MATLAB [18].

The third measure consists of fractal dimensions. We start with covering the attractor by a hierarchy of boxes with sides proportional to 2^{-k}, $k = 0, 1, 2, \ldots$. To be efficient, a tree structure

is used to book these boxes. Let $\mathcal{B}_k$ denote the number of nonempty boxes at level k, and $\rho_{k,j}$ denote the proportion of the attractor contained in the j^{th} box of level k. The capacity and information dimensions are defined, in principle, as the limits:

$$\begin{aligned} D_C &= \lim_{k\to\infty} \frac{\log_2 \mathcal{B}_k}{k}, && \text{(Capacity)}, \\ D_I &= \lim_{k\to\infty} \frac{-\Sigma_j(\rho_{k,j}\log_2 \rho_{k,j})}{k}, && \text{(Information)}. \end{aligned} \tag{19}$$

In practice, the sequence of data appearing in the righthand side of (19) are available only for the first few k's (say, $k \leq 12$). So, these limits are again to be estimated by means of linear correlation. However, these sample data sometimes present a piecewise linear profile, and cause some ambiguity about the linear correlation. This uncertainty can be measured by performing the related box counting with several representations of the given attractor generated by different initial conditions.

3. WORKED EXAMPLES AND DISCUSSIONS

In this section, we shall show several sample applications of the methods presented in Section 2. The aim is to complete a bifurcation diagram which reveals the dynamic behavior of an FHN system in the presence of a sinusoidal forcing term. It turns out that such an aim is partially subject to the finite-precision character of computers, when exotic bifurcation phenomena are encountered.

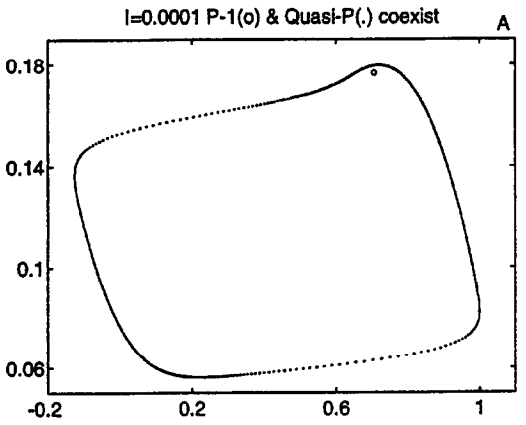

(a) Coexistent P-1(o) and quasi-periodic ($\cdots$) attractors at $I = 0.0001$.

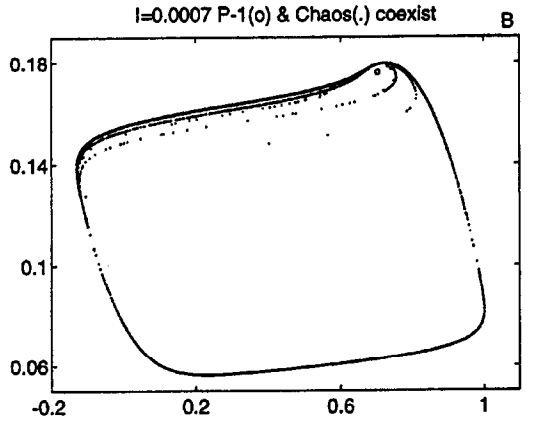

(b) Coexistent P-1(o) and chaotic ($\cdots$) attractors at $I = 0.0007$.

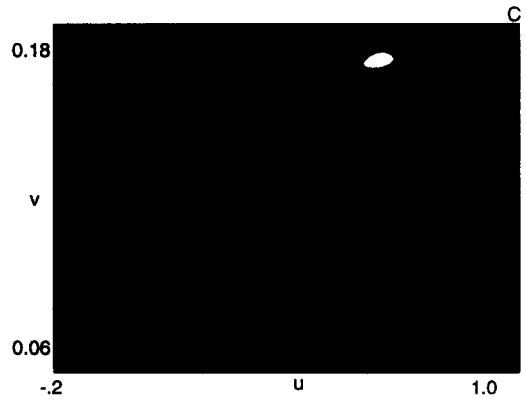

(c) Domains of attraction corresponding to (a). White area is related to the P-1 attractor.

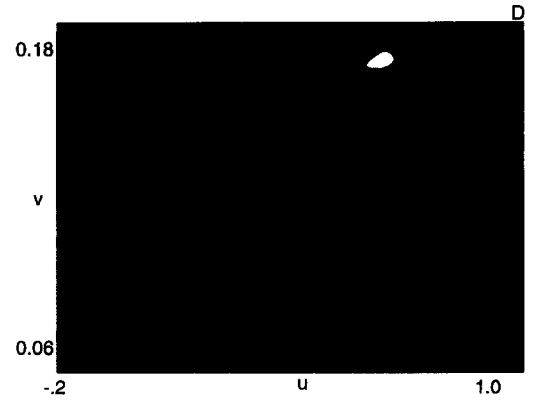

(d) Domains of attraction corresponding to (b). White area is related to the P-1 attractor.

Figure 1. Onset of the forced FHN system with control parameters listed in (20).

In what follows, the control parameters in FHN equations (1),(2) are set as

$$(\alpha, \beta, \theta, \gamma, I_o) = (0.25, 0.02, 0.25, 0.1, 0.082). \tag{20}$$

For $I = 0$, the autonomous FHN system characterized by (20) is bistable in that a stable steady state is coexistent with a stable relaxation oscillation, as demonstrated in detail in our previous work [6]. The relaxation oscillation in question has period $2\pi T_o = 200$, so the perturbation frequency γ specified in (20) is such that $\gamma \cdot T_o \approx 3$.

If $I \neq 0$, the period of a possible periodic solution to (1) and (2) is restricted to the form $2\pi\lambda/\gamma$, λ is a natural number. We shall call it a P-λ solution, if any.

Now we start to increase I from zero. The steady state of the original system is seen to evolve into a P-1 solution. The coexistent relaxation oscillation is seen to become quasi-periodic, and then chaotic. The difference between quasiperiodicity and chaos is judged here by the first Lyapunov exponent, ℓ_1. Namely, $\ell_1 \sim 0$ for the former, while $\ell_1 > 0$ for the latter. See Figure 1 for the geometry of these attractors as projected onto a Poincaré section, and of their respective domains of attraction.

As I is increased further, the chaotic motion is seen to be merged into a P-3 solution, but still coexistent with the original P-1 solution. When a P-λ solution has been identified by Poincaré map for some fixed I, we can extend the solution path, in the direction with I either increasing or decreasing, by the continuation techniques described in Section 2.4 until the stability concern (15) is met. In that case the Poincaré map as implemented in Sections 2.1 to 2.3 is called again to search other attractors.

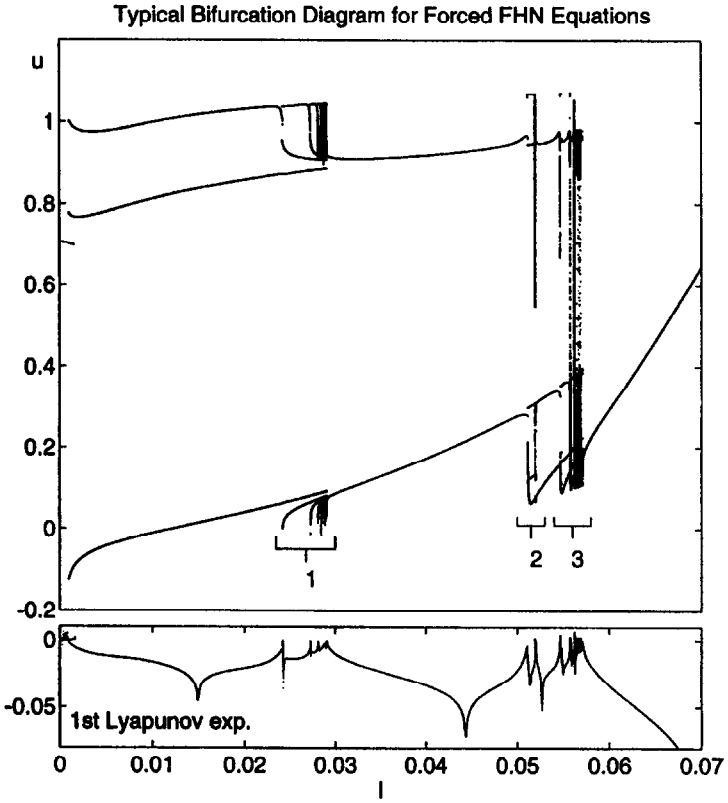

Figure 2. Overall bifurcation diagram for the forced FHN system with control parameters listed in (20). The upper box presents u versus I under Poincaré map. Also indicated are three portions to be blown up in next figures. The lower box presents the first Lyapunov exponent versus I.

According to this procedure, we find a sequence of $\lambda \to \lambda + 2$, period-adding bifurcation started with $\lambda = 1$. By this we mean when a P-λ solution becomes unstable as detected by

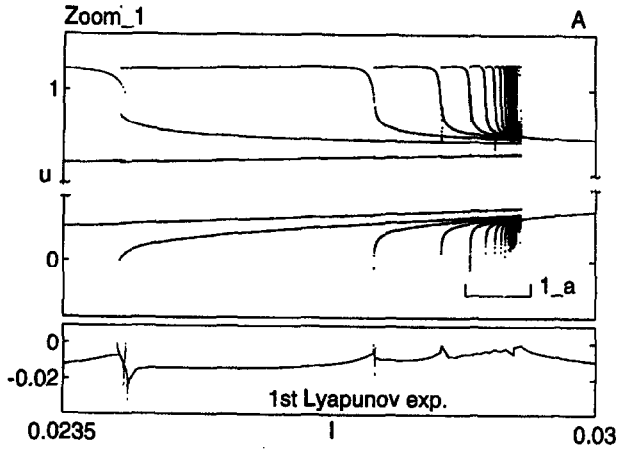

(a) Blowup of Portion 1 of Figure 1.

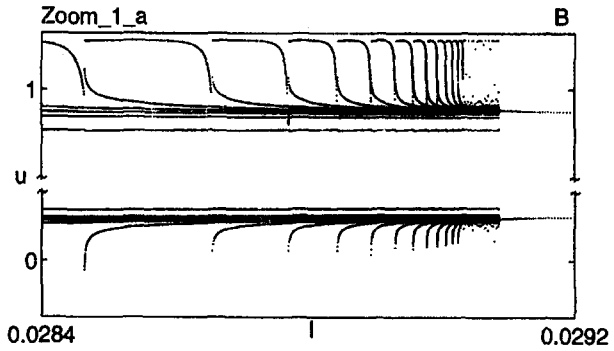

(b) Blowup of Portion 1_a of (a).

Figure 3.

the numerical continuation, there exists instead a stable P-$(\lambda+2)$ solution. The above observed coexistence phenomenon still takes place around the bifurcation points. In other words, we are encountered with hysteretic bifurcation. The scenario and several of its successive blowups are shown in Figures 2 and 3. The typical domains of attraction of competitive P-3 and P-5, due to hysteresis, as well as P-5 and P-7 are shown in Figures 4 and 5, respectively. Note that these different attractors may become of little difference in part. Computations should be performed with care.

Let I_λ denote the starting I of the P-$(2\lambda+1)$ branch of the above bifurcation. We find by extrapolation that

$$\lim_{\lambda\to\infty}\frac{I_{\lambda+1}-I_\lambda}{I_\lambda-I_{\lambda-1}}=0.680. \tag{21}$$

Therefore, this period-adding phenomenon ends up at some finite I, say I_*. According to the convergence rate (21) and the limitation of computer precision, it is hard in practice to find tiny P-$(2\lambda+1)$ branches for sufficiently large λ. For instance, we have found a P-131 branch with I almost all equal to I_*.

Immediately after I_*, we find another type of period-adding bifurcation. The event can be sorted into several levels. The top level is a sequence of $\lambda\to\lambda+1$, period-adding started with $\lambda=2$. Using I_λ again to denote the starting I of the P-λ branch of this sequence, we have this time the extrapolated limit

$$\lim_{\lambda\to\infty}\frac{I_{\lambda+1}-I_\lambda}{I_\lambda-I_{\lambda-1}}=0.676. \tag{22}$$

In contrast to the previous one, the successive branches of the present sequence are disjoint. The gap between P-λ and P-$(\lambda+1)$ branches is partially filled by a P-$(2\lambda+1)$ branch for any λ. These partial fillings form the second level.

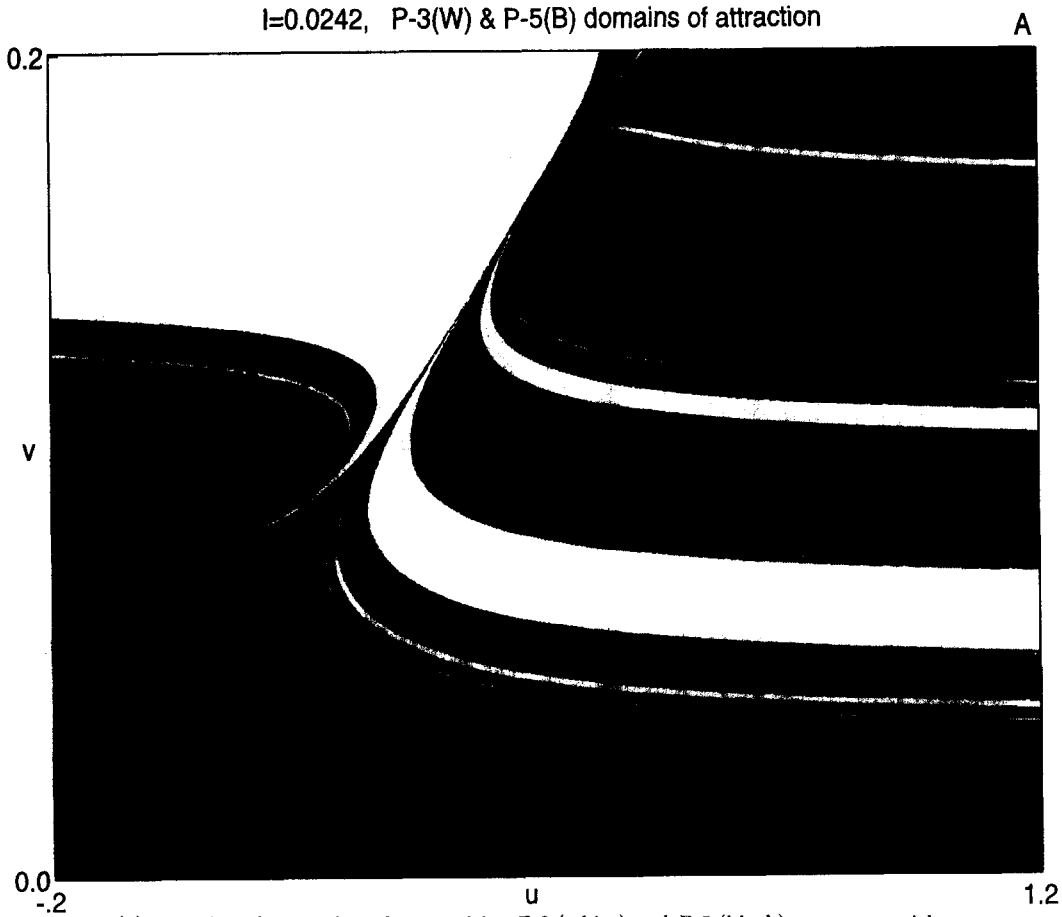

(a) Domains of attraction of competitive P-3 (white) and P-5 (black) attractors with $I = 0.0242$.

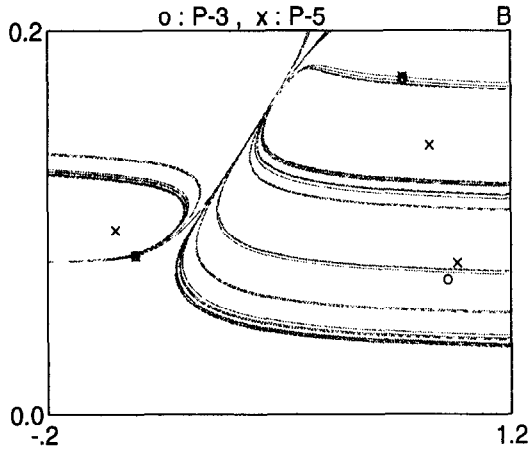

(b) Locations of the P-3(o) and P-5(×) attractors and the related boundary of domains of attraction.

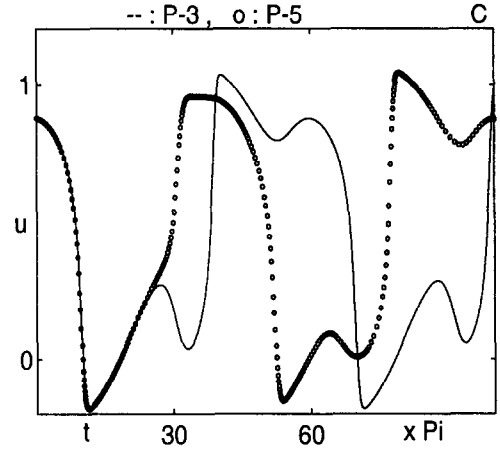

(c) The u-history of P-3(−) and P-5(oo) attractors starting with negligible difference.

Figure 4.

More detailed computations reveal that the associated bifurcation diagram is refined from $\lambda \to \lambda + 1$ to $\lambda \to 2\lambda + 1 \to \lambda + 1$ to $\lambda \to 3\lambda + 1 \to 3\lambda + 2 \to \lambda + 1$. Namely, we are encountered with multilevel $m \to m + n \to n$, period-adding in between.

Of course, this pattern is coupled with certain irregularities brought about by chaos and hysteresis. The scenario and several of its successive blowups are shown in Figures 2, 6 and 7. An

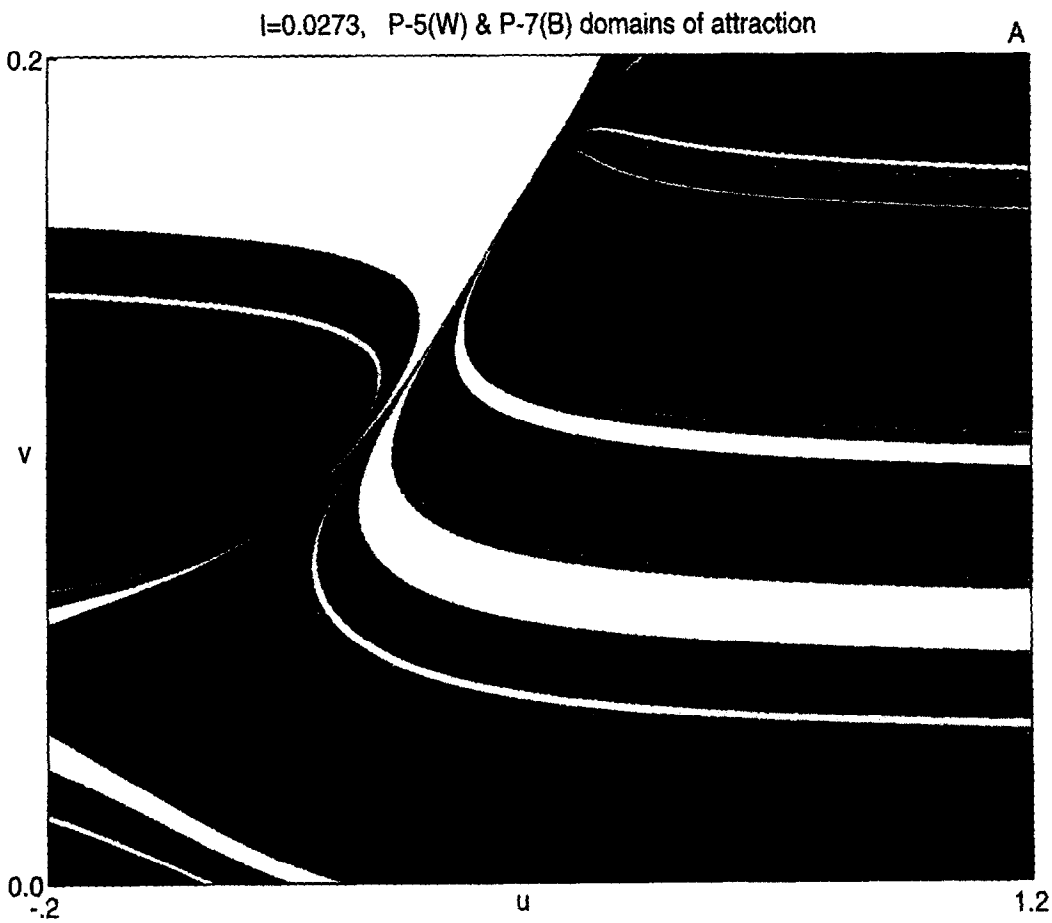

(a) Domains of attraction of competitive P-5 (white) and P-7 (black) attractors with $I = 0.0273$.

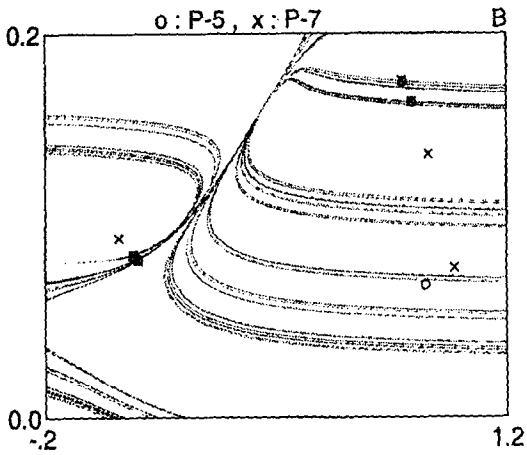

(b) Locations of the P-5(o) and P-7(×) attractors and the related boundary of domains of attraction.

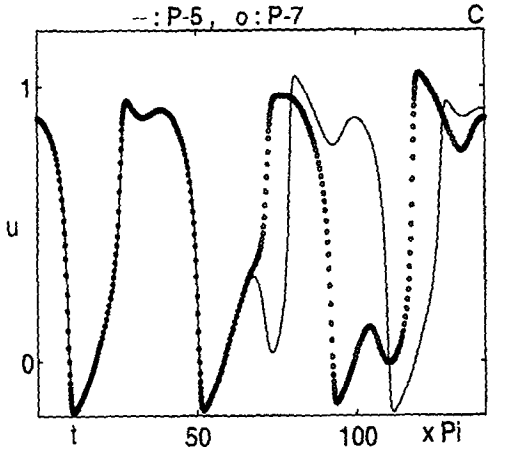

(c) The u-history of P-5(−) and P-7(oo) attractors starting with negligible difference.

Figure 5.

example of hysteresis is seen during the period-adding between P-2 and P-3 branches. Figure 8 shows the typical domains of attraction of competitive P-2 and P-5 attractors. Note again the partial coincidence between these different attractors.

So far, the issue of bifurcation is discussed in terms of Poincaré map and numerical continuation. We shall show next that power spectrum is also a powerful tool in this regard. Figure 9 presents

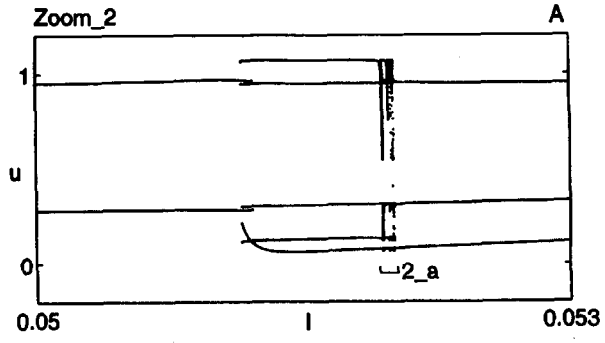

(a) Blowup of Portion 2 of Figure 1.

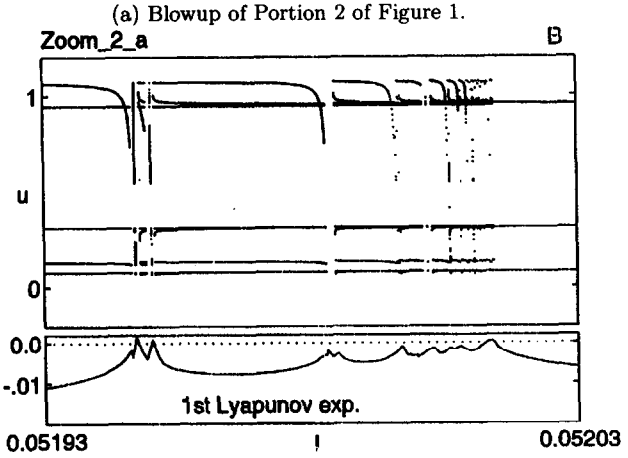

(b) Blowup of Portion 2_a of (a).

Figure 6.

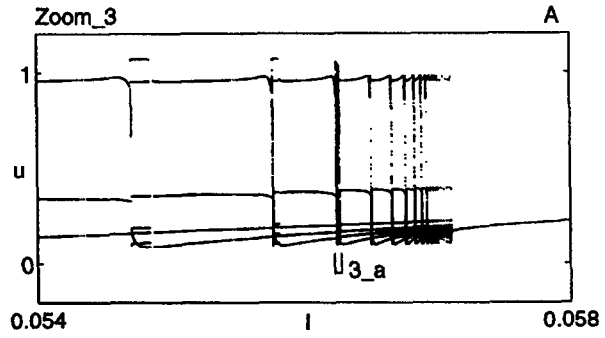

(a) Blowup of Portion 3 of Figure 1.

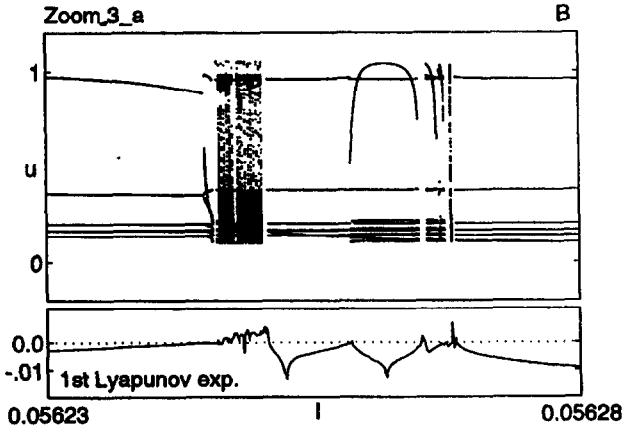

(b) Blowup of Portion 3_a of (a).

Figure 7.

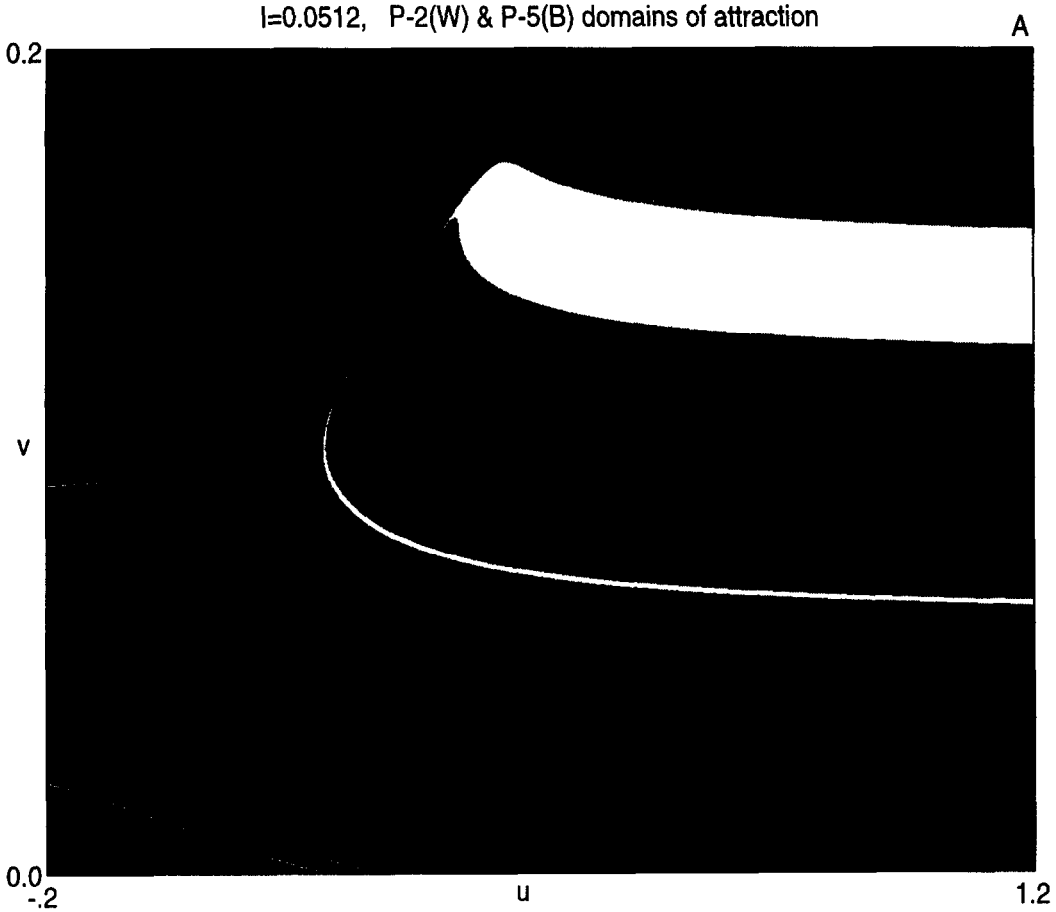

(a) Domains of attraction of competitive P-2 (white) and P-5 (black) attractors with $I = 0.0512$.

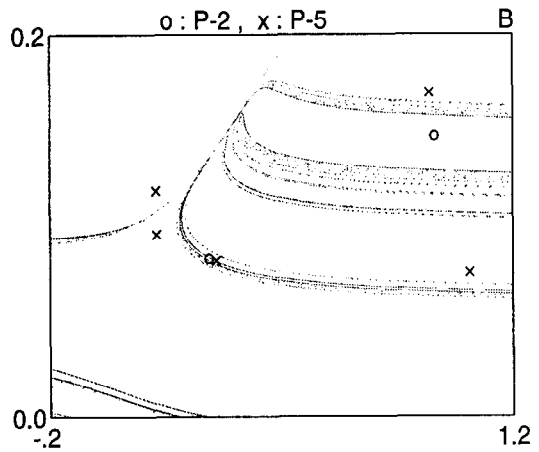

(b) Locations of the P-2(o) and P-5(×) attractors and the related boundary of domains of attraction.

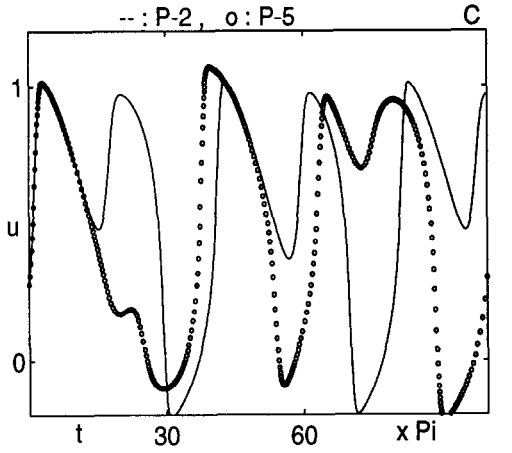

(c) The u-history of P-2(−) and P-5(oo) attractors starting with negligible difference.

Figure 8.

several sample power spectra related to the first, or $\lambda \to \lambda + 2$, type of period-adding bifurcation, including the aperiodic motion at the outset. It is easy to see that a P-λ attractor presents $\lambda - 1$ regular peaks even if λ is sufficiently large. Aperiodicity is evidenced by irregular peaks or interpeak noise. Similar results are shown in Figure 10 for the second, or for brevity $\lambda \to 2\lambda + 1 \to \lambda + 1$, type of bifurcation.

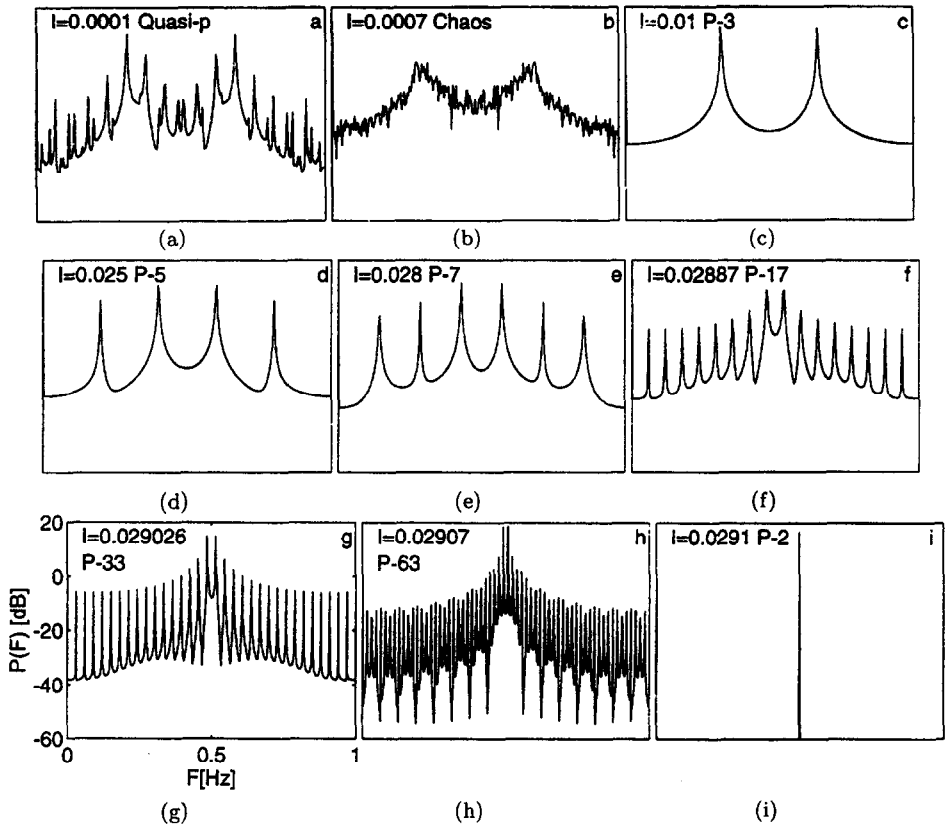

Figure 9. Sample power spectra of $\lambda \rightarrow \lambda + 2$, period-adding bifurcation.

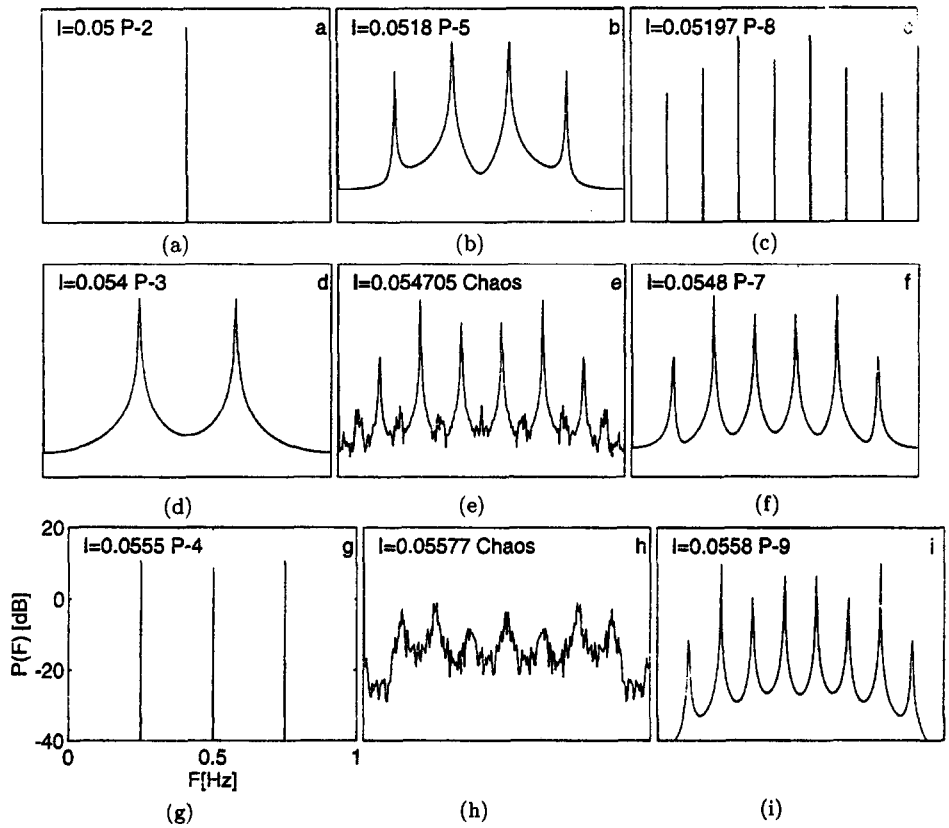

Figure 10. Sample power spectra of $\lambda \rightarrow 2\lambda + 1 \rightarrow \lambda + 1$, period-adding bifurcation.

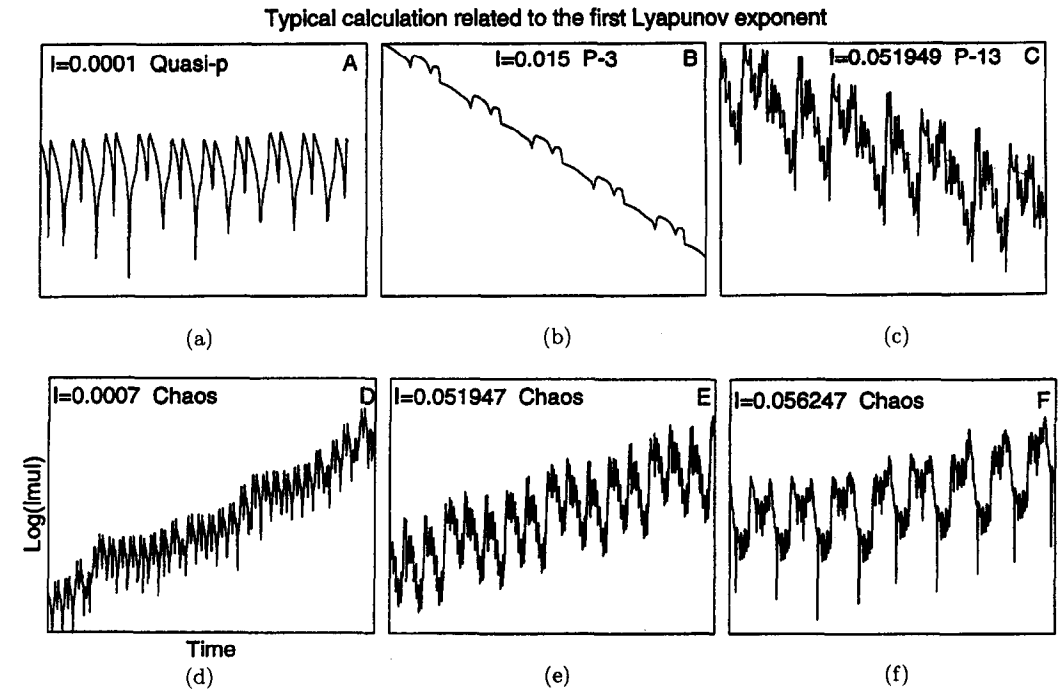

Figure 11. Sample plots of $\log|\mu_1(t)|$ versus t in connection with (17). The slope of linear correlation in each plot is used to approximate the first Lyapunov exponent, ℓ_1. (a) quasi-periodic; (b) and (c) periodic; (d)–(f) chaos.

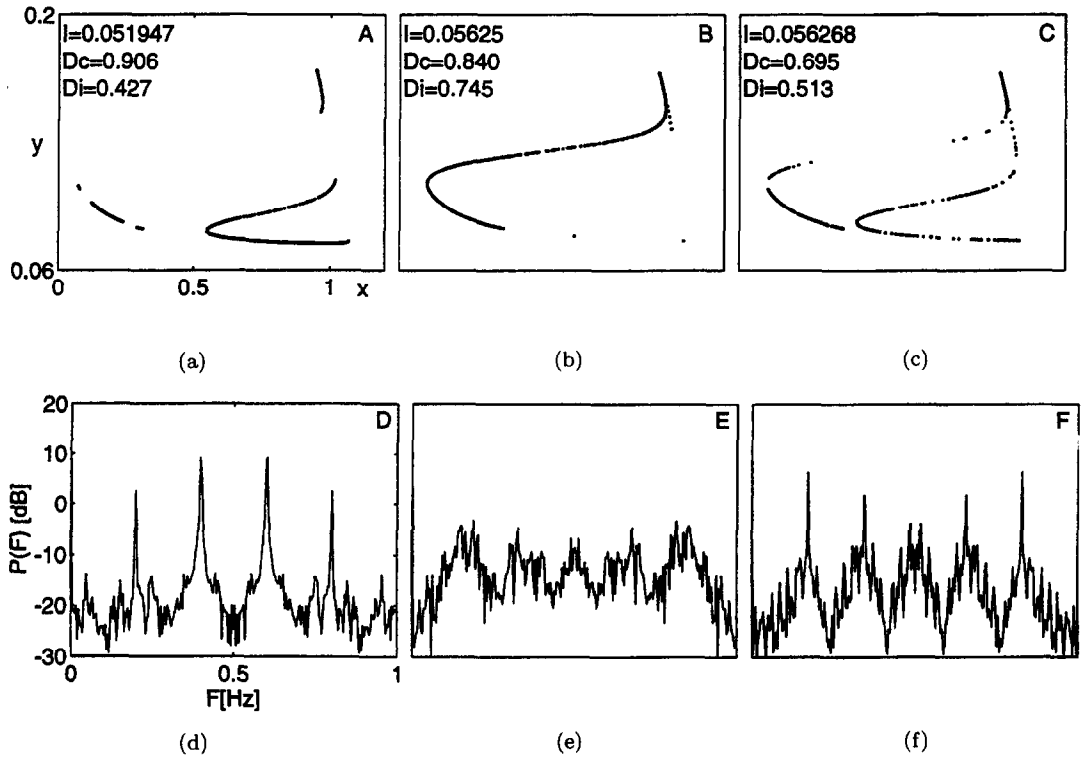

Figure 12. (a)–(c) Sample plots of chaotic attractors; (d)–(f) their respective power spectra.

We now come to discuss the estimation of Lyapunov exponents, especially the first exponent since we are dealing with two-dimensional systems. Figure 11 presents several sample plots of $\log|\mu_1(t)|$ versus t as suggested by (17). The oscillatory feature of these plots indicates the limit ℓ_1

does not exist in mathematical sense. Nevertheless, the still well-behaved pattern allows us to interpret ℓ_1 in terms of linear correlation. The sign of ℓ_1 as determined in this way is consistent with the attractor's behavior. Namely, $\ell_1 > 0$ for chaos; < 0 for periodic cases. In particular, (18) holds almost exactly. The overall plot of ℓ_1 versus I is shown in Figure 2. Some blowups are shown in Figures 3, 6 and 7.

As for the geometry of chaotic attractors, we show several sample plots in Figure 12, together with their respective power spectra. Within each chaotic attractor, the phase points are not uniformly spaced. This fact is also shown in Figure 7b. To be more quantitative, Figure 13 presents the capacity and information dimensions with respect to the most readable, yet chaotic, part of Figure 7b. The shaded area in this figure indicates the uncertainty of performing such computations as explained in Section 2.

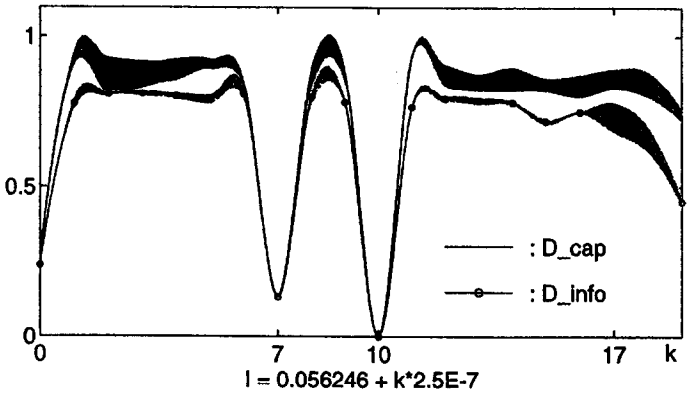

Figure 13. Fractal dimensions (— capacity, —o— information) varied with I corresponding to the most readable, yet chaotic, part of Figure 7b. Possible error is indicated by the shaded area.

For I greater than the limit I^* determined by (22), the applied sinusoidal forcing term becomes dominant, and harmonic resonance (i.e., P-1 solution) sets in afterwards.

In conclusion, we have presented a rather complete bifurcation diagram in connection with the sinusoidally forced FHN system. If the forcing frequency is comparable with the natural frequency of the underlying autonomous system, complex period-adding phenomena can take place as the forcing magnitude is increased from zero.

REFERENCES

1. R. FitzHugh, Impulses and physiological states in theoretical models of nerve membrane, *Biophysical Journal* **1**, 445–466 (1961).
2. J.S. Nagumo, S. Arimoto and S. Yoshizawa, An active pulse transmission line simulating nerve axon, *Proc. IRE* **50**, 2061–2070 (1962).
3. A.L. Hodgkin and A.F. Huxley, A quantitative description of membrane current and its application to conduction and excitation in nerve, *J. Physiol. (London)* **117**, 500–544 (1952).
4. J. Rinzel, Models in neurobiology, In *Mathematical Aspects of Physiology, Lects. in Appl. Math. 19*, (Edited by F.C. Hoppensteadt), pp. 281–297, Amer. Math. Soc., Providence, RI, (1981).
5. J.D. Murray, *Mathematical Biology, Biomathematics 19*, Springer-Verlag, (1989).
6. M.H. Chou, Computer-aided experiments on the Hopf bifurcation of the FitzHugh-Nagumo nerve model, *Computers Math. Applic.* **29** (10), 19–33 (1995).
7. B. Van der Pol and J. Van der Mark, Frequency demultiplication, *Nature* **120** (3019), 363–364 (1927).
8. M.P. Kennedy and L.O. Chua, Van der Pol and chaos, *IEEE Trans. Circuits Syst.* **CAS-33** (10), 974–980 (1986).
9. A.C. Hindmarsh, ODEPACK, a systematized collection of ODE solvers, In *Scientific Computing*, (Edited by R.S. Stepleman *et al.*), pp. 55–64, North-Holland, (1983).
10. D. Kahaner, C. Moler and S. Nash, *Numerical Methods and Software*, Prentice Hall, (1989).
11. B.H. Tongue, On obtaining global nonlinear system characteristics through interpolated cell mapping, *Physica* **28D**, 401–408 (1987).
12. C.S. Hsu, *Cell-to-Cell Mapping: A Method of Global Analysis for Nonlinear Systems*, Springer-Verlag, (1987).

13. M.H. Chou, A modified cell-to-cell mapping method for nonlinear systems, *Computers Math. Applic.* **25** (8), 47–57 (1993).
14. M.H. Chou, Hopf bifurcation in a reaction-diffusion system governed by the FitzHugh-Nagumo equations, *Computers Math. Applic.* **23** (10), 85–97 (1992).
15. J.E. Dennis, Jr. and R.B. Schnabel, *Numerical Methods for Unconstrained Optimization and Nonlinear Equations*, Prentice Hall, (1983).
16. H.B. Keller, *Lectures on Numerical Methods in Bifurcation Problems*, Tata Institute of Fundamental Research, (1987).
17. G.L. Baker and J.P. Gollub, *Chaotic Dynamics: An introduction*, Cambridge Univ. Press, (1990).
18. T.P. Krauss, L. Shure and J.N. Little, *Signal Processing Toolbox for Use with MATLAB*, The MathWorks Inc., (1994).